Nuclear Materials and Energy 39 (2024) 101674

Contents lists available at ScienceDirect

Nuclear Materials and Energy

journal homepage: www.elsevier.com/locate/nme

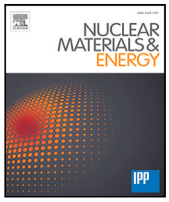

Effect of grain size on defect annealing in displacement-damaged tungsten

Anže Založnik [a,*], David Dellasega [b,c], Gabriele Alberti [b], Matteo Passoni [b,c], Thomas Schwarz-Selinger [d], Marlene I. Patino [a], Michael J. Simmonds [a], Matthew J. Baldwin [a], George R. Tynan [a]

[a] Center for Energy Research, University of California at San Diego, La Jolla, CA, USA
[b] Dipartimento di Energia, Politecnico di Milano, Milan, Italy
[c] Istituto per la Scienza e Tecnologia dei Plasmi, CNR, Milan, Italy
[d] Max–Planck-Insitut für Plasmaphysik, Garching, Germany

ARTICLE INFO

Keywords:
Tungsten
Annealing
Deuterium
Retention
Nanograin
Grain boundary

ABSTRACT

Pulsed laser deposition and subsequent thermal treatment were used to create compact tungsten layers with various grain sizes (1 μm, 100 nm, and 10 nm). The layers were self-damaged at room temperature up to 0.23 dpa using 20.3 MeV W ions and annealed in vacuum at 473 K or 673 K prior to exposure to deuterium plasma to populate the surviving displacement defects. Thermal desorption spectroscopy was used to measure deuterium retention and study the desorption profile. Rate-equation modeling of the desorption spectra was performed to study the behavior of individual traps at both annealing temperatures. After annealing the 1 μm and 100 nm samples at 473 K, the deuterium retention was found to decrease by 24% and 9%, respectively, whereas the total deuterium retention in the 10 nm sample did not change. Annealing at 673 K reduced total deuterium retention by additional 27%, 14%, and 34% in the case of the samples with a grain size of 1 μm, 100 nm, and 10 nm, respectively.

1. Introduction

As a planned plasma-facing material in future fusion devices, tungsten (W) will be subject to high fluxes of energetic particles, such as hydrogen isotopes (HIs), helium, and neutrons. These particles will affect the properties of the material, creating bubbles, blisters, swelling, embrittlement, displacement damage, etc. Displacement damage, such as vacancies, interstitials, and dislocations, has been shown by many studies to strongly enhance HI retention in W (e.g. [1–3]), since defects in the crystal lattice act as strong binding sites for HIs, and a single defect is often capable of trapping multiple HI particles [4–6]. This represents an economical and a safety issue, due to the loss of fusion fuel and the radioactive nature of tritium.

Molecular dynamics [7–9], density functional theory [10–12], thermodynamical [13] calculations, as well as experimental observations [12,14] show that grain boundaries (GBs) can trap and provide fast-diffusion channels for HIs, with the diffusion barrier similar or lower than that in the bulk [7,10,15–17]. The preferential diffusion along the GBs was found to be a consequence of the activation barrier for diffusion back into the bulk being much higher than the diffusion barrier along the GB [10]. However, not all GBs exhibit such properties as the exact kinematic properties depend on the type and orientation of the GB in question.

In addition to being trapping sites for HIs, GBs can also act as sinks for point defects [16,18,19], therefore exhibiting the ability to anneal certain mobile defects and lower their concentration in the material. Consequently, materials with smaller grain sizes and therefore higher density of GBs are believed to be more radiation resistant [20,21] and are attributed certain self-healing properties [18,20,22]. In [22], three stages of self-healing of nano-grained material were described. First, highly mobile interstitials get trapped at GBs, which act as sinks for interstitials, therefore strongly reducing their concentration. For many materials this happens already at room temperature. Second, when the temperature rises, the GBs start acting as interstitial sources, releasing the trapped interstitials back into the bulk where they can recombine with vacancies in the region close to the GB. This reduces the concentration of vacancies in the material. Third, when the temperature is high enough for the vacancies to become mobile, they too, as interstitials before, diffuse and get trapped at the GBs, strongly reducing their concentration. By contrast, the interstitials in single-crystal W readily recombine with the vacancies they encounter during their random walk, thus initially reducing the concentration of both defect types [16]. However, due to the lack of GBs in single-crystals, the self-healing stages of nano-grained materials are not observed.

* Corresponding author.
E-mail address: azaloznik@ucsd.edu (A. Založnik).

https://doi.org/10.1016/j.nme.2024.101674
Received 15 March 2024; Received in revised form 3 May 2024; Accepted 14 May 2024
Available online 17 May 2024

The self-healing behavior is of course strongly temperature-dependent, since the defects are required to be mobile to anneal at GBs. Many experiments studying the effects of temperature on defect annealing in W have been conducted over the years. Such experiments mostly focus on the effects of post-annealing in vacuum [23–26] or on simultaneous annealing and damaging [23,27,28]. More recent studies focus on the synergistic effects of simultaneous D exposure and annealing on the evolution of defects [29], whereas studies on the effect of GBs on annealing efficiency are sparse. In [19] the authors annealed nano-grained W samples at 473 K and 573 K. Only after annealing at 573 K, the temperature at which mono-vacancies are believed to already be mobile, was the concentration of vacancies reduced, whereas annealing at 473 K had no effect on the amount of vacancies in the sample. In this paper we study the defect annealing efficiency of W layers with different grain sizes, varying from 10 nm to 1 μm. Annealing was performed at 473 K and 673 K. These temperatures were chosen because 473 K is still considered too low for significant mono-vacancy mobility, whereas at 673 K mono-vacancies are highly mobile. Samples were exposed to deuterium (D) plasma and analyzed by thermal desorption spectroscopy (TDS). Rate-equation modeling allowed us to deduce annealing efficiency for individual trap types as a function of annealing temperature and the average grain size of the sample.

2. Experiment

Pulsed laser deposition (PLD) [30] was used to deposit 12 W layers on flat circular polycrystalline W substrates with a diameter of 6 mm. The substrates were annealed at 1273 K for 1 h prior to deposition. During PLD, a laser pulse with a fluence of 15 J/cm^2 is focused in a vacuum chamber on a 2 inch W target. Due to the laser-matter interaction, W is ablated at high energy (100 eV/atom) and expands in the vacuum chamber (base pressure 10^{-3} Pa). W target is properly moved (translation and rotation) to ensure uniform ablation of the surface. The expanding W species are deposited on the W substrates placed 7 cm away in front of the target at room temperature (no intentional heating is applied). The W film grows with a deposition rate of about 15 nm/min. For our samples the planned layer thickness was 3 μm and the average grain size 10 nm. To grow the grains to a larger size, some of the samples were thermally treated in vacuum with a base pressure of 10^{-5} Pa. Four samples were thermally treated at 1023 K for a duration of 2 h, and an additional four samples at 1223 K also for 2 h, resulting in the average grain size of 100 nm and 1 μm, respectively. To reach the maximal temperature and to cool down the samples after the thermal treatment, a linear ramp of 20 K/min was used. This entire procedure resulted in three batches of four samples with different grain size distributions. In this paper the samples with the average grain size of 10 nm, 100 nm, and 1 μm will be labeled W-10, W-100, and W-1000, respectively.

Three samples from each batch were irradiated by 20.3 MeV W^{6+} ions at room temperature to introduce displacement damage into the deposited layers. According to SRIM2013 [31] and assuming the properties of bulk W, the damaged region extended down to 2.3 μm with a peak at about 1.35 μm. The evaluated damage dose at the peak was 0.23 dpa corresponding to a measured fluence of 7.8×10^{17} W/m^2. The beam was raster scanned across the surface to get a laterally homogeneous irradiation. The average W ion flux was 7×10^{13} W/m^{2}s which corresponds to a dose rate of 2×10^{5} dpa/s. The damage dose was calculated by evaluating the 'vacancy.txt' file of the 'Ion Distribution and Quick Calculation of Damage' option of SRIM2013. The value of the displacement threshold energy was set to 90 eV.

Two of the three damaged samples from each batch were then annealed in vacuum at the base pressure of around 10^{-6} Pa, one at 473 K and the other at 673 K. The annealing was done in a quartz tube with an infrared heat source. The temperature was measured by a K-type thermocouple in direct contact with the side of the sample. A temperature ramp of 0.3 K/s was used to reach the set temperature, after which the sample was kept at that temperature for 1 h before letting it cool down freely. Table 1 summarizes the steps taken in preparation of all 12 samples.

Table 1
Properties and preparation steps for the samples used in this study. Asterisks indicate the samples used in the EBSD analysis.

	PLD W		
	As deposited (W-10)	Thermally treated at 1023 K (W-100)	Thermally treated at 1223 K (W-1000)
Nominal grain size	10 nm	100 nm	1 μm
Undamaged	1	1[a]	1[a]
Damaged with 20.3 MeV W^{6+}	1	1	1
Damaged + annealed at 473 K	1	1	1
Damaged + annealed at 673 K	1[a]	1[a]	1

[a] EBSD analysis.

The undamaged W-100 and W-1000 samples, and the W-10 and W-100 samples annealed at 673 K, were analyzed by electron backscatter diffraction (EBSD) to measure the grain size distributions and to check that the process of annealing did not considerably change the grain sizes. In Table 1 these samples are indicated with an asterisk. The analysis was performed on a Thermo Scientific Apreo Scanning Electron Microscope (SEM) with an Oxford Instruments Symmetry EBSD detector. The samples were mounted at a 70° tilt and a 20 kV accelerating voltage was used.

All samples were then exposed to D plasma in the PISCES-RF linear plasma device [32] to a flux of D ions of around 3×10^{22} D/m^{2}s as measured by an RF compensated fast-reciprocating single Langmuir probe. Each exposure lasted for 1 h for a fluence of around 1.1×10^{26} D/m^2. The values of other plasma parameters, measured by the probe, were 3×10^{18} m^{-3} for the electron density, 5 eV for the electron temperature, and 15 V and 5 V for the floating and space potential, respectively. The samples were biased to −40 V, resulting in around 45 eV of energy carried by D ions, which was kept low to minimize the effect of the D super-saturated layer [33]. The samples were mounted on a water-cooled sample manipulator with a K-type thermocouple in direct contact with the back of the sample. The samples heated up to around 335 K due to interaction with plasma. The time needed to reach this equilibrium temperature was around 3 min. All plasma conditions are summarized in Table 2.

Finally, the D content and desorption profile were measured by TDS in the same setup that was previously used for annealing. Each sample was heated up to 1273 K with a linear temperature ramp of 0.3 K/min. A residual gas analyzer (RGA), was used to monitor the desorbing species in the range of 1–4 amu. Mass 3 (HD) and 4 (D_2) were used in the analysis of D desorption. After each measurement the RGA was calibrated by a calibrated leak standard (LACO Technologies) with a known D_2 leak rate of 2.15×10^{-10} mol/s and an uncertainty of 5.4%. The same calibration factor was assumed for both D_2 and HD molecules.

Table 2
Plasma conditions during D plasma exposure.

Floating potential	15 V
Space potential	5 V
Bias	−40 V
Energy	45 eV
Electron density	3×10^{18} m^{-3}
Electron temperature	5 eV
Ion flux	3×10^{22} D/m^{2}s
Ion fluence	1.1×10^{26} D/m^2
Temperature	335 K

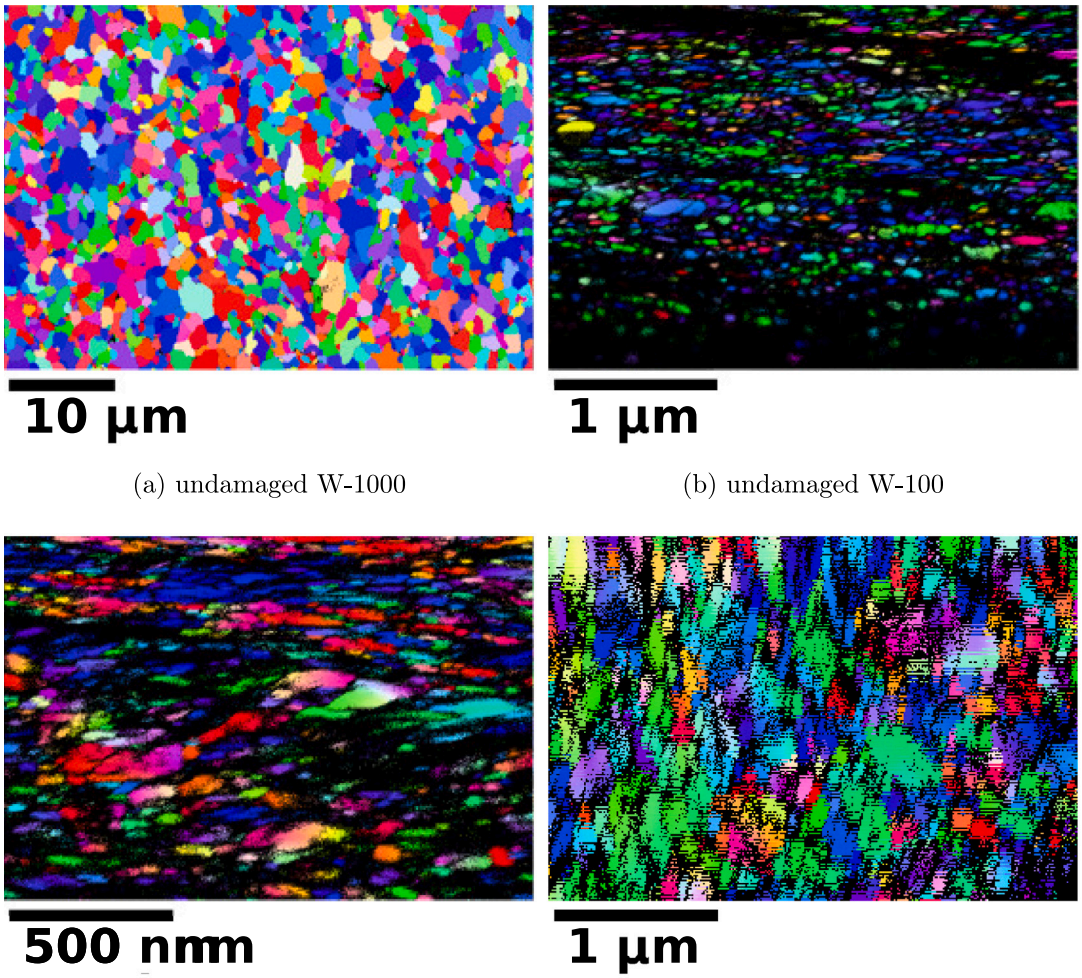

(a) undamaged W-1000 (b) undamaged W-100

(c) W-10, annealed at 673 K (d) W-100, annealed at 673 K

Fig. 1. EBSD images of undamaged and annealed samples. False color represents grain orientation, while black pixels are not identifiable.

3. Results and discussion

3.1. EBSD analysis

Since the W-100 and W-1000 samples were thermally treated at 1023 K and 1223 K to grow the grains, subsequent annealing at 473 K and 673 K was not expected to considerably change the grain size distribution. To verify this, the grain size distributions were measured by the EBSD technique for the undamaged W-100 and W-1000 samples, and the W-10 and W-100 samples that were damaged and then annealed at 673 K. Fig. 1 shows the grain orientation maps. Due to the limited spatial resolution of the EBSD setup and possible surface roughness of the samples (the layers had not been polished after deposition), there is a high concentration of unassigned (black) pixels visible in the images of samples with sub-micron grain size. These pixels indicate locations at which the diffraction pattern could not be recognized and therefore the technique was unable to determine the orientation of the grain. In the case of undamaged W-100, 80% of pixels were unassigned, while in the case of the damaged and annealed W-10 and W-100, 69% and 46% pixels were unassigned, respectively. A higher percentage of unassigned pixels introduces higher uncertainty in the grain size distribution.

Grain orientation maps in Fig. 1 were used to determine the grain size distributions. The size of each individual grain was measured along two axes. The long axis was determined by finding the longest distance between any two points within the same grain. The short axis was then determined as the longest distance between two points within the grain, perpendicular to the long axis. The average grain size in each direction was then calculated for each measured sample. Fig. 2 shows the resulting grain size distributions and average grain sizes along the long and the short axis for the analyzed samples. The average grain size was found to increase slightly, from 110 nm to 142 nm along the long and from 27 nm to 49 nm along the short axis, for the W-100 sample after annealing at 673 K for 1 h. This increase is not significant with respect to the average grain sizes of the other two samples. The undamaged W-1000 sample had the average grain size along the long axis of 1.3 µm and the annealed W-10 sample 17 nm. This indicates that even for the W-10 layers, which were not thermally treated to grow the grains, annealing at 673 K for 1 h does not significantly change the average grain size from the nominal value. However, it is important to emphasize that grain size distributions and average grain sizes carry a large uncertainty due to the high percentage of unassigned pixels.

3.2. TDS spectra and total D amounts

The TDS spectra show four distinguishable peaks, therefore four corresponding deuterium trap types were assumed to exist in the material. The positions of the peaks are indicated in Fig. 3, where the spectra of undamaged, damaged, and both annealed W-1000 samples are shown. Trap type I has a corresponding peak position around 450 K and is often associated with trapping in dislocations and/or grain boundaries [34,35]. The peak between 500 K and 650 K (trap II) is most often associated with deuterium release from mono-vacancies [28,

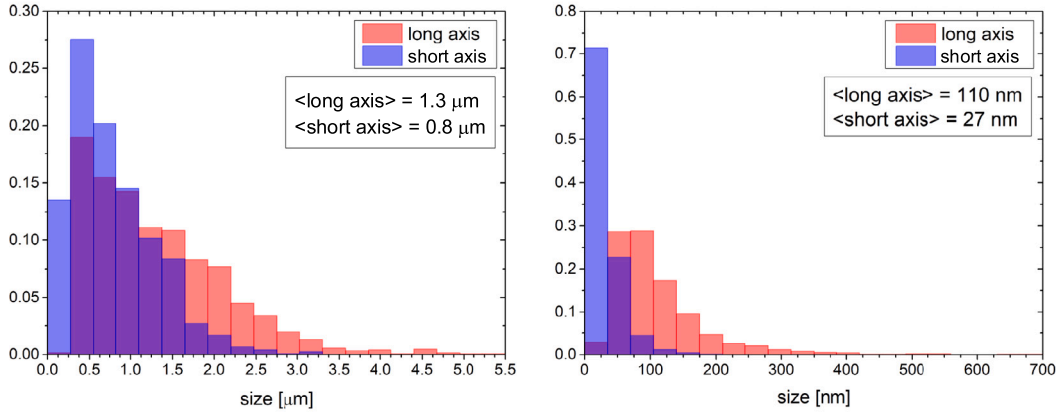

(a) undamaged W-1000 (b) undamaged W-100

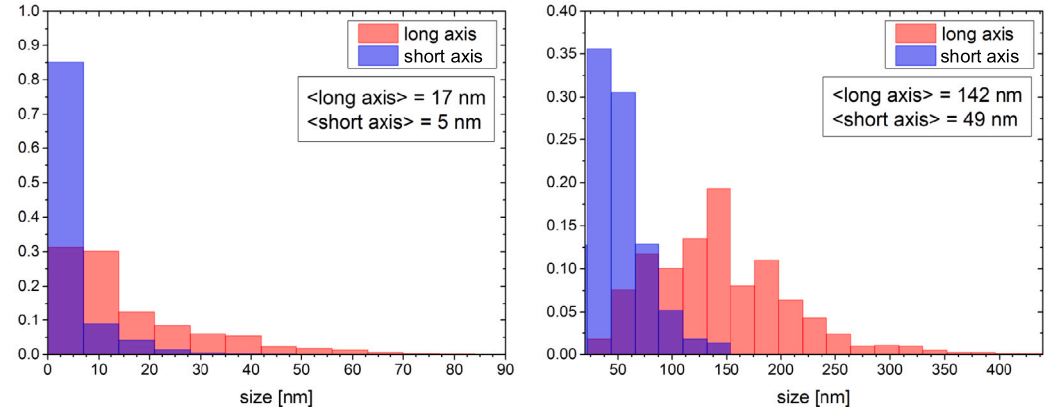

(c) W-10, annealed at 673 K (d) W-100, annealed at 673 K

Fig. 2. Grain size distributions and average grain sizes along the long and the short axis of undamaged samples and samples annealed at 673 K.

36]. In the attempt to produce predominantly mono-vacancies Zibrov et al. [37] irradiated W samples with 10 keV D^+ ions up to 6.3×10^{-3} dpa, which resulted in a peak somewhat below 600 K when heated up with a rate of 0.25 K/s. When irradiating with 9 MeV W ions up to 1.1 dpa [38], the main TDS peak shifted to around 670 K (trap III), which likely corresponds to D de-trapping from small vacancy clusters. A strong peak corresponding to trap III also appeared in a study by Simmonds et al. [29], where he annealed self-damaged W samples at 673 K while simultaneously exposing them to D plasma. However, this trap type has not been identified in that study. Trap type IV with a corresponding broad peak positioned between 700 K and 950 K is usually associated with de-trapping from large vacancy clusters [28,36]. It is important to emphasize that most defects in W have been shown to be able to trap multiple deuterium atoms in a single defect, resulting in broad TDS peaks that can strongly overlap with other various trap types. Assigning TDS peaks to individual defects is therefore a very simplistic approach, though a separate treatment of individual peaks (albeit possibly corresponding to various trap types) can still be beneficial for the analysis of annealing effects. Therefore we will still refer to individual peaks as trap types throughout this paper.

Figs. 4a–d show the experimental TDS spectra (dots) and the best fits (lines) for all W-10, W-100, and W-1000 samples and the corresponding total D amounts. The fits are obtained by simulating the TDS phase of the experiment, as described later in Section 3.3. The low-temperature peak at around 450 K (trap I) is the most prominent peak in all TDS spectra of the undamaged samples and its intensity

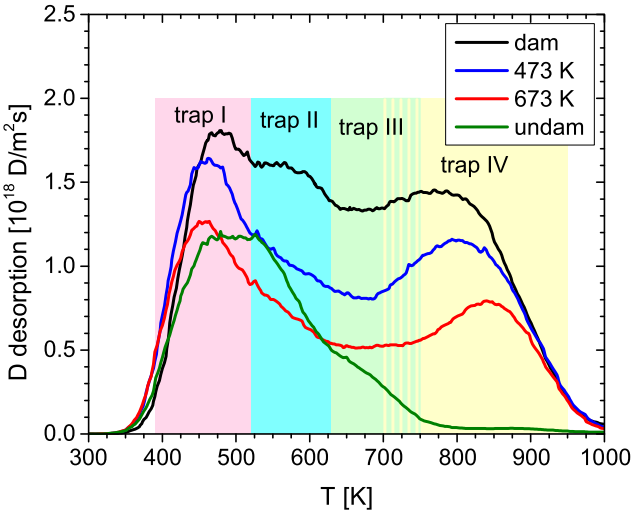

Fig. 3. TDS spectra of the undamaged (green), damaged (black), and annealed (blue and red) W-1000 samples. The positions of four distinguishable peaks are also indicated. (For interpretation of the references to color in this figure legend, the reader is referred to the web version of this article.)

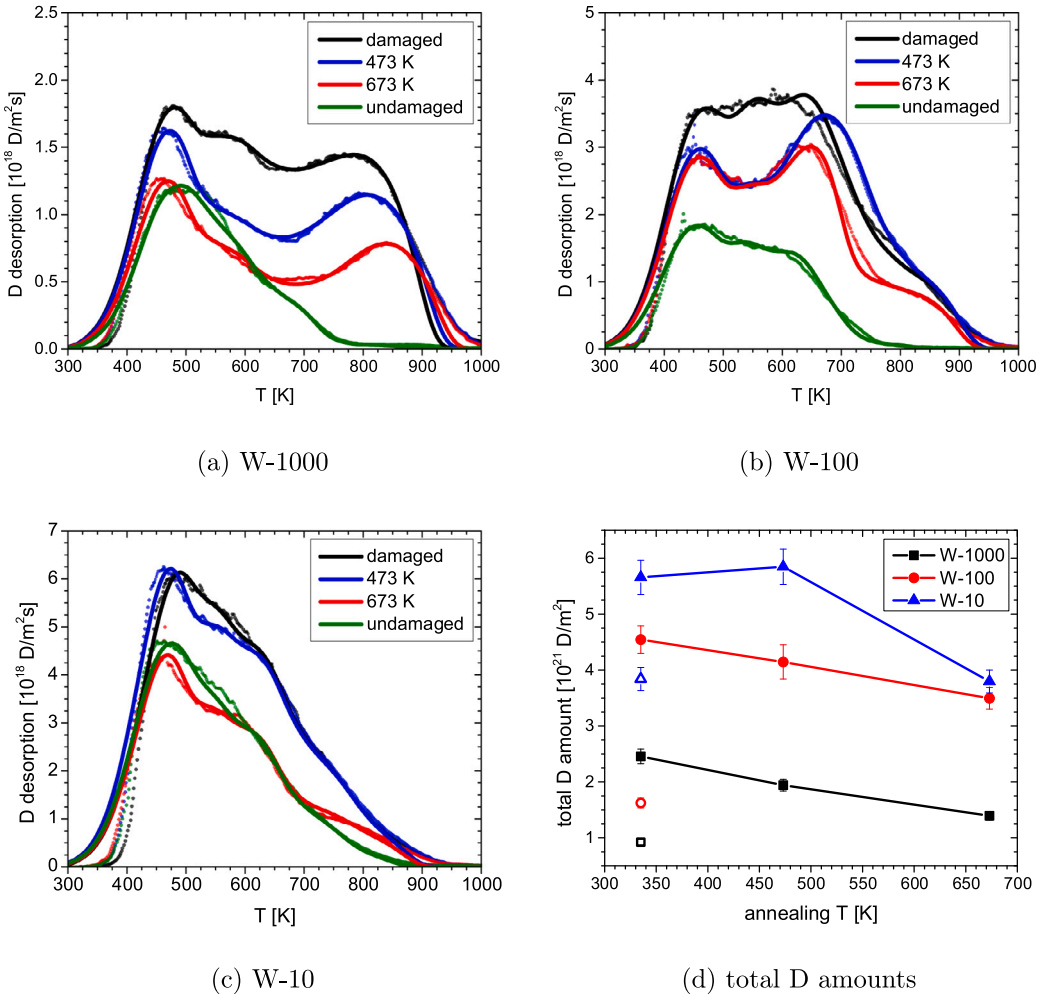

Fig. 4. Experimental TDS spectra (dots) and modeling results (lines) for all (a) W-1000, (b) W-100, and (c) W-10 samples. (d) Total D amounts as a function of annealing temperature. Undamaged (open symbols) and damaged/unannealed samples are plotted at the plasma exposure temperature (335 K).

drops significantly with the increase of the grain size. Therefore, it is reasonable to assume trap I is associated with D trapping in GBs, since the density of GBs increases as the grain size decreases. However, the fact that the intensity of this peak changes with damaging and annealing indicates that the peak must also be associated with an additional displacement defect type, since the grain sizes of the samples should not change significantly during damaging. The concentration of trap IV in the undamaged samples is very low, indicating that there are very few intrinsic vacancy clusters in our samples. The total D amounts in the undamaged samples, calculated by integrating the TDS spectra, amount to $(3.8 \pm 0.2) \times 10^{21}$ D/m^2, $(1.62 \pm 0.09) \times 10^{21}$ D/m^2, and $(9.24 \pm 0.05) \times 10^{20}$ D/m^2 for W-10, W-100, and W-1000, respectively. The data follows the previously observed trends [39], namely that the samples with smaller grain sizes show higher hydrogen isotope retention. However, one should note that in our case this trend is intensified by the thermal treatment of the W-100 and W-1000 samples, which probably annealed some of the existing intrinsic defects.

High-energy W irradiation introduced a significant amount of new traps of type II, III, and IV relative to trap I in all three damaged and unannealed samples, as seen in Fig. 4. It appears that larger grain size favors a creation of larger defect clusters (trap type IV), as the highest-temperature peak shows the strongest increase in the W-1000 sample and the weakest in the W-10 sample. The calculated total D amounts are $(5.7 \pm 0.3) \times 10^{21}$ D/m^2, $(4.5 \pm 0.2) \times 10^{21}$ D/m^2, and $(2.5 \pm 0.1) \times 10^{21}$ D/m^2 for W-10, W-100, and W-1000, respectively, which is consistent with previous observations [14,40]. As Frenkel pairs are produced during the damaging, the highly mobile self-interstitials readily diffuse and recombine with the created vacancy-type defects. The steady-state defect concentration is therefore a result of competition between damage creation and active recombination. Since samples with smaller grain sizes exhibit additional sinks for defects in the form of GBs, fewer interstitials survive and are available to recombine with vacancies. The resulting concentration of vacancy-type defects is therefore higher.

Annealing of the W-1000 (Fig. 4(a)) samples follows a well-known trend seen in other studies where coarse-grained W samples were annealed in vacuum (e.g. [24,25,29]), namely that the concentration of all defects decreases monotonically with the annealing temperature. The total D amounts after annealing at 473 K and 673 K are $(1.9 \pm 0.1) \times 10^{21}$ D/m^2 and $(1.39 \pm 0.08) \times 10^{21}$ D/m^2, respectively. Compared to $(2.5 \pm 0.1) \times 10^{21}$ D/m^2 in the case of the unannealed sample, this represents a 24% and 44% decrease in total D retention in the case of annealing at 473 K and 673 K, respectively.

In the case of the smallest grain size (Fig. 4(c)), annealing the W-10 samples at 473 K and 673 K resulted in a total D retention of $(5.8 \pm 0.3) \times 10^{21}$ D/m^2 and $(3.8 \pm 0.2) \times 10^{21}$ D/m^2, respectively, whereas the retention in the unannealed sample was $(5.7 \pm 0.3) \times 10^{21}$ D/m^2. Interestingly, there was little change in the shape of the TDS spectra of the W-10 sample annealed at 473 K compared to the unannealed sample. Moreover, the total D retention shows a slight increase, however the calculated values are the same within their uncertainties. Annealing at 673 K reduced the total D amount by 33%. This behavior can be explained by a high density of GBs in the W-10 samples. Annealing of displacement

damage has been shown to occur in stages [41–43]. Stage II takes place roughly between 100 K and 623 K with various annealing sub-stages, attributed to the release of self-interstitials from different traps with a wide range of interaction energies [43]. At temperatures above 623 K (stage III), the mono-vacancies become increasingly mobile in W. Some authors propose an even lower onset temperature for mono-vacancy mobility of around 550 K [44,45], meaning they can diffuse throughout the material and anneal at surfaces, grain boundaries, dislocations, etc. As explained earlier, high GB density of the W-10 samples leaves the sample depleted of self-interstitials after displacement damaging. Therefore, annealing at 473 K (stage II) has little effect on defect concentration. On the other hand, annealing at 673 K (stage III) is much more efficient, since the high density of GBs provides many sinks for the mobile mono-vacancies.

Finally, annealing the W-100 samples at 473 K and 673 K (Fig. 4(b)) resulted in $(4.1 \pm 0.3) \times 10^{21}$ D/m^2 and $(3.5 \pm 0.2) \times 10^{21}$ D/m^2 of retained D, respectively. The D retention in the unannealed sample was $(4.5 \pm 0.2) \times 10^{21}$ D/m^2, yielding a 9% decrease in the case of annealing at 473 K and a 23% decrease in the case of annealing at 673 K. Similarly to the W-1000 samples, annealing of the W-100 samples results in a monotonic decrease of the total defect concentration, although the decrease was found to be slightly more gradual with increasing temperature. Annealing at 473 K (stage II) is therefore less efficient compared to the W-1000 sample and more efficient compared to the W-10 sample. This can again be explained by the amount of surviving self-interstitials during the damaging. Since more self-interstitials anneal during the damaging of a W-100 sample compared to a W-1000 sample, fewer are available to recombine with vacancy-type defects during the stage II annealing. However, due to the lower GB density compared to the W-10 samples, the concentration of surviving self-interstitials is larger and therefore the annealing somewhat more efficient. One might expect stage III annealing at 673 K to be more efficient compared to the W-1000, again due to the higher density of GBs acting as sinks for the mobile mono-vacancies. Interestingly, this was found not to be the case. Comparing total D amounts of the samples annealed at 473 K and 673 K, the retention decreased by 15% in the case of the W-100 sample and by 27% in the case of the W-1000 sample, making the stage III annealing of W-1000 more efficient. Moreover, comparing the TDS spectra in Fig. 4, we can see that annealing the W-100 sample at 673 K only reduced the concentrations of traps III and IV compared to the sample annealed at 473 K, whereas the change in traps I and II is negligible.

3.3. Modeling

In order to study the effect of annealing on individual trap types, a rate-equation model implemented in the TESSim code [46] was used to model the TDS spectra. Four trap types were assumed, each capable of accepting multiple deuterium atoms per trap site. It was found that assuming two deuterium atoms per trap for each trap type was sufficient to produce good fits to the TDS spectra. The de-trapping attempt frequency was chosen to be $\nu = 10^{13}$ s^{-1}, the diffusion coefficient for deuterium $D_0 = 1.9/\sqrt{2} \times 10^{-7}$ m$^{2/s}$, and the migration barrier $E_m = 0.2$ eV [5]. The simulated thickness of the samples was 3 μm with a 2 μm uniform damaged layer. Only the TDS phase of the experiment was simulated, assuming that all traps are initially fully populated with D atoms. No attempt has been made to model the differences in GB densities and diffusion along the GBs. Trap concentrations and de-trapping energies were varied when trying to find the best fit to the experimental TDS spectra. The de-trapping energies mostly match between all samples, with only minor variations in some cases to ensure a good quality of the fits. The only larger deviations from the average de-trapping energies were observed in the case of trap IV of the W-1000 samples and trap III of the W-100 samples.

Table 3 shows the de-trapping energies for all W-1000 samples. As can be seen in Fig. 4(a), the highest-temperature peak in the TDS spectra gradually shifts to higher temperatures as the annealing temperature is increased. This required us to increase the de-trapping energies of the corresponding trap in our model to produce the peak at the correct temperature.

Table 3
De-trapping energies (in [eV]) for W-1000 samples and all four trap types. The exact values are given for the damaged sample and the deviations from these values for the rest of the samples.

	Damaged	Undamaged	473 K	673 K
Trap I	1.07	+0.03	–	–
	0.97	+0.02	–	–
Trap II	1.32	–	–	–
	1.2	–	–	–
Trap III	1.6	–	–	–
	1.45	–	–	–
Trap IV	1.9	+0.2	+0.04	+0.01
	1.74	+0.1	+0.02	+0.09

Table 4
De-trapping energies (in [eV]) for W-100 samples and all four trap types. The exact values are given for the damaged sample and the deviations from these values for the rest of the samples.

	Damaged	Undamaged	473 K	673 K
Trap I	1.02	–	–	–
	0.92	–	–	–
Trap II	1.35	–	–	–
	1.17	–	–	–
Trap III	1.55	–	–	−0.08
	1.43	–	–	−0.03
Trap IV	1.92	–	–	–
	1.71	–	–	–

Table 5
De-trapping energies (in [eV]) for W-10 samples and all four trap types. The exact values are given for the damaged sample and the deviations from these values for the rest of the samples.

	Damaged	Undamaged	473 K	673 K
Trap I	1.02	–	−0.02	−0.02
	0.94	−0.02	−0.02	−0.02
Trap II	1.32	–	–	–
	1.15	–	–	–
Trap III	1.62	–	–	–
	1.47	–	–	–
Trap IV	1.9	–	–	–
	1.72	–	–	–

In the case of the W-100 samples, the de-trapping energies are shown in Table 4. Fig. 4(b) shows a change in the peak position in the case of the W-100 sample annealed at 673 K. The shifting peak corresponds to trap III and interestingly shifts to lower desorption temperature as the annealing temperature increases. Again, to correctly capture the peak position in our model, the de-trapping energies needed to be adjusted in this case.

Finally, the de-trapping energies for the W-10 samples are shown in Table 5. In this case, the de-trapping energies were found to be consistent regardless of the annealing temperature, with only minor variation to ensure a good fit.

The trap concentrations for each sample and each trap type are given in Fig. 5. As expected, all trap types in the W-1000 samples decrease monotonically in concentration as the annealing temperature increases (Fig. 5(a)). The annealing is strongest for trap II and trap III, which after annealing at 673 K decreased in concentration by 65% and 72%, respectively, with the strongest decrease after the stage II annealing. Traps I and IV were found to anneal more gradually, reducing their concentration after annealing at 673 K by 37% and 36%, respectively. As mentioned before, the trap IV peak shifted to higher desorption temperature as the annealing temperature increased. This is

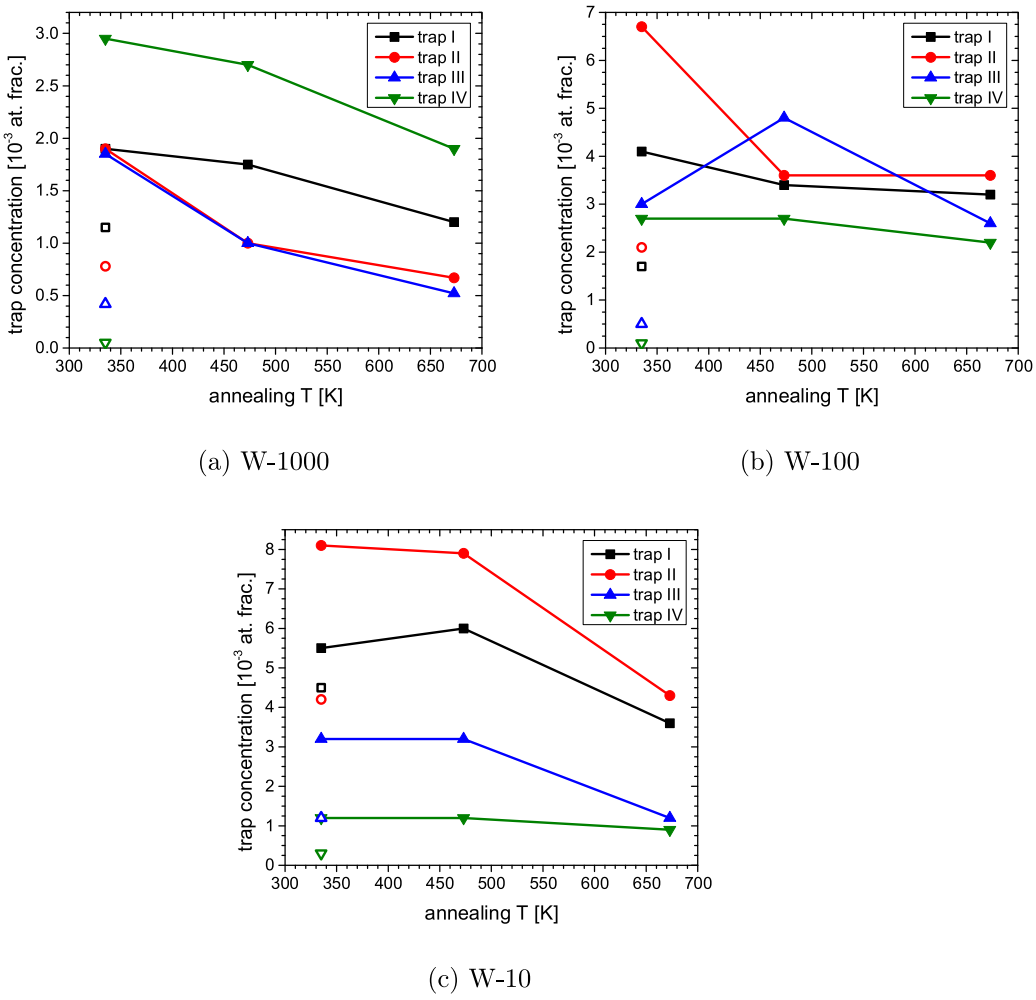

Fig. 5. Trap concentrations for (a) W-1000, (b) W-100, and (c) W-10 samples as a function of annealing temperature. Undamaged (open symbols) and damaged/unannealed samples are plotted at the plasma exposure temperature (335 K).

probably due to the smaller vacancy clusters annealing more efficiently or growing into the larger clusters. The growth of large vacancy clusters has been observed by Zibrov [47], where the average positron lifetime in the positron annihilation spectroscopy (PAS) was shown to increase for samples annealed at various temperatures up to 800 K. The shift in the TDS spectra can be explained by the results of the molecular dynamic (MD) simulations in [6]. While the binding energy itself does not change considerably as a vacancy cluster grows, a larger number of D atoms is trapped at fill-levels with higher binding energy in larger clusters. As the cluster distribution shifts to larger sizes, the TDS peak should shift toward higher temperatures while maintaining a similar high-temperature tail due to the similar highest de-trapping energy, as observed in our TDS spectra of the W-1000 samples.

As already discussed, we see almost no change in the concentration of any trap type after annealing a W-10 sample at 473 K (Fig. 5(c)), which is explained by the lack of self-interstitials and low mobility of the existing defects. However, the TDS spectrum (Fig. 4(c)) and modeling do show a small reduction of trap II. This could be due to a small number of self-interstitials that did survive the capture at GBs during the process of damaging, or due to very low mobility of mono-vacancies (trap II). Since the mobility has an Arrhenius dependence on temperature, its value at 473 K can be low, but non-zero. After annealing at 673 K a strong decrease of traps I, II, and III was observed, reducing their concentration by 35%, 47%, and 63%, respectively. Such strong annealing of mono-vacancies (trap II) is expected due to their enhanced mobility in the environment with a high density of GBs. Annealing of small vacancy clusters (trap III) can also be explained by their dissociation and subsequent annealing of resulting mono-vacancies at GBs. The concentration of large vacancy clusters (trap IV), however, only decreased by 8%, since much higher temperature is needed for their dissociation [47]. In contrast to the W-1000 samples, no shift of the peak corresponding to trap IV was observed for the W-10 samples. While the shift of the size distribution of vacancy clusters to larger sizes can occur due to annealing of smaller and survival of larger clusters, or due to the growth of the smaller clusters into larger, both of these phenomena are greatly inhibited in a sample with a high density of GBs. Since clusters are still immobile at these annealing temperatures, the annealing has to be a result of recombination between a cluster and multiple self-interstitials, which, as discussed earlier, are strongly reduced in the W-10 samples. Moreover, the growth of the clusters is a result of mono-vacancy diffusion and agglomeration, the rate of which is strongly reduced by mono-vacancies annealing at GBs. Therefore, no noticeable shift to larger vacancy clusters has been observed.

The W-100 samples show a very interesting behavior as they are annealed at 473 K and 673 K (Fig. 5(b)). During annealing at 473 K, the concentration of traps I and II decreases by 17% and 46%, respectively. The concentration of trap IV remains the same, whereas the concentration of trap III increases by 60%. As a result of this, the shape of the TDS spectrum changes considerably compared to the damaged/unannealed sample. Since stage II annealing assumes only recombination with released self-interstitials, it is hard to imagine that such a phenomenon could lead to an increase in trap concentration.

However, if we assume a low but non-negligible mobility of mono-vacancies, as is possibly indicated by the results on W-10 samples, and considering their high initial concentration, we could explain the increase in the concentration of small vacancy clusters (trap III) by agglomeration of mono-vacancies. This would also explain a sharp decrease of mono-vacancy concentration (trap II), since it offers an additional pathway for their annealing. The reason why such behavior is not observed in the W-10 sample is that agglomeration is inhibited by a high density of GBs, therefore slowly mobile mono-vacancies preferentially anneal at GBs rather than agglomerate to form clusters. Annealing at 673 K has preserved the shape of the TDS spectrum, with little to no annealing of traps I and II, whereas the decrease of traps III and IV was found to be 85% and 19%, respectively, compared to the sample annealed at 473 K. Additionally, the trap III peak shifted to lower desorption temperature by about 25 K. Strong trap III annealing can again be explained by the dissociation of small vacancy clusters. This provides an additional source of mono-vacancies, the result of which is a competition between mono-vacancy production and capture at GBs. Since the density of GBs is much lower compared to the W-10 samples, the rate of annealing is strongly reduced and the resulting reduction in concentration seems to be balanced by the production of mono-vacancies through the dissociation of small clusters. It is important to point out that the explanation of the annealing of the W-100 samples is highly speculative and additional studies are needed to offer an explanation with higher confidence.

4. Conclusions

Tungsten samples with three different grain sizes (1 μm, 100 nm, and 10 nm) were self-damaged and annealed at 473 K and 673 K. The samples with the largest grain size (1 μm) show a previously observed behavior of coarse-grained W, where the concentration of defects decreases monotonically as the annealing temperature increases. The highest-temperature peak in the TDS spectra, usually associated with deuterium de-trapping from vacancy clusters, shifts to higher desorption temperatures as the annealing temperature increases, indicating the annealing and/or growth of smaller vacancy clusters. In the case of the smallest grain size (10 nm), the samples show weak annealing at 473 K, which can be explained by the lack of self-interstitials after damaging a material with a high density of GBs. Annealing at 673 K showed a reduction of all trap types, consistent with the increased mobility of mono-vacancies and the dissociation of small vacancy clusters at this temperature. In the case of the samples with the grain size of 100 nm, the TDS spectrum was found to considerably change the shape after annealing at 473 K, consistent with the growth of small vacancy clusters. Moreover, annealing at 673 K had little effect on the trap types with lower de-trapping energies, which could be explained by the interplay of mono-vacancy annealing at GBs and their production by the dissociation of small vacancy clusters. Overall, annealing at 673 K reduced total D retention by 44%, 22%, and 33% in the case of a grain size of 1 μm, 100 nm, and 10 nm, respectively. At first glance it might be surprising that coarser-grained W seems to be more efficient at annealing of displacement defects, however one has to take into account the lack of self-interstitials in nano-grained W after damaging, leading to extremely inefficient stage II annealing.

CRediT authorship contribution statement

Anže Založnik: Writing – original draft, Investigation, Formal analysis, Conceptualization. **David Dellasega:** Writing – review & editing, Resources. **Gabriele Alberti:** Writing – review & editing, Resources. **Matteo Passoni:** Writing – review & editing, Resources. **Thomas Schwarz-Selinger:** Writing – review & editing, Resources. **Marlene I. Patino:** Writing – review & editing, Investigation, Formal analysis. **Michael J. Simmonds:** Writing – review & editing, Investigation. **Matthew J. Baldwin:** Writing – review & editing, Supervision, Funding acquisition. **George R. Tynan:** Writing – review & editing, Supervision, Funding acquisition.

Declaration of competing interest

The authors declare that they have no known competing financial interests or personal relationships that could have appeared to influence the work reported in this paper.

Data availability

Data will be made available on request.

Acknowledgments

This work was supported by US-DOE-FES under agreement DE-SC0022528.

References

[1] B. Tyburska, V. Kh. Alimov, O.V. Ogorodnikova, K. Schmid, K. Ertl, Deuterium retention in self-damaged tungsten, J. Nucl. Mater. 395 (2009) 150.
[2] M.H.J. 't Hoen, M. Mayer, A.W. Kleyn, H. Schut, P.A. Zeijlmans van Emmichoven, Reduced deuterium retention in self-damaged tungsten exposed to high-flux plasmas at high surface temperatures, Nucl. Fusion 53 (2013) 043003.
[3] T. Schwarz-Selinger, A critical review of experiments on deuterium retention in displacement-damaged tungsten as function of damaging dose, Mater. Res. Express 10 (2023) 102002.
[4] K. Heinola, T. Ahlgren, K. Nordlund, J. Keinonen, Hydrogen interaction with point defects in tungsten, Phys. Rev. B 82 (2010) 094102.
[5] N. Fernandez, Y. Ferro, D. Kato, Hydrogen diffusion and vacancies formation in tungsten: Density Functional Theory calculations and statistical models, Acta Mater. 94 (2015) 307.
[6] J. Hou, X.-S. Kong, X. Wu, J. Song, C.S. Liu, Predictive model of hydrogen trapping and bubbling in nanovoids in BCC metals, Nature Mater. 18 (2019) 833.
[7] U. von Toussaint, S. Gori, A. Manhard, T. Höschen, C. Höschen, Molecular dynamics study of grain boundary diffusion of hydrogen in tungsten, Phys. Scr. T145 (2011) 014036.
[8] Y. Yu, Y. Shu, Y.-N. Liu, G.-H. Lu, Molecular dynamics simulation of hydrogen dissolution and diffusion in a tungsten grain boundary, J. Nucl. Mater. 455 (2014) 91.
[9] P.M. Piaggi, E.M. Bringa, R.C. Pasianot, N. Gordillo, M. Panizo-Laiz, J. del Río, C. Gómez de Castro, R. González-Arrabal, Hydrogen diffusion and trapping in nanocrystalline tungsten, J. Nucl. Mater. 458 (2015) 233.
[10] H.-B. Zhou, Y.-L. Liu, S. Jin, Y. Zhang, G.-N. Luo, G.-H. Lu, Investigating behaviours of hydrogen in a tungsten grain boundary by first principles: from dissolution and diffusion to a trapping mechanism, Nucl. Fusion 50 (2010) 025016.
[11] W. Xiao, W.T. Geng, Role of grain boundary and dislocation loop in H blistering in W: A density functional theory assessment, J. Nucl. Mater. 430 (2012) 132.
[12] C. González, M. Panizo-Laiz, N. Gordillo, C.L. Guerrero, E. Tejado, F. Munnik, P. Piaggi, E. Bringa, R. Iglesias, J.M. Perlado, R. González-Arrabal, H trapping and mobility in nanostructured tungsten grain boundaries: a combined experimental and theoretical approach, Nucl. Fusion 55 (2015) 113009.
[13] T. Oda, Thermodynamic model for grain boundary effects on hydrogen solubility, diffusivity and permeability in poly-crystalline tungsten, Fusion Eng. Des. 112 (2016) 102.
[14] S. Markelj, J. Zavašnik, A. Šestan, T. Schwarz-Selinger, M. Kelemen, E. Punzón-Quijorna, G. Alberti, M. Passoni, D. Dellasega, Deuterium retention and transport in ion-irradiated tungsten exposed to deuterium atoms: Role of grain boundaries, Nucl. Mater. Energy 38 (2024) 101589.
[15] U. von Toussaint, S. Gori, Modeling hydrogen transport in large disordered systems, Nucl. Fusion T159 (2014) 014058.
[16] G. Valles, M. Panizo-Laiz, C. González, I. Martin-Bragado, R. González-Arrabal, N. Gordillo, R. Iglesias, C.L. Guerrero, J.M. Perlado, A. Rivera, Influence of grain boundaries on the radiation-induced defects and hydrogen in nanostructured and coarse-grained tungsten, Acta Mater. 122 (2017) 277.
[17] A. Manhard, U. von Toussaint, P. Sand, M. Stienecker, Visualizing spatially inhomogeneous hydrogen isotope diffusion by hydrogenography, Nucl. Mater. Energy 36 (2023) 101498.
[18] X.-M. Bai, A.F. Voter, R.G. Hoagland, M. Nastasi, B.P. Uberuaga, Efficient annealing of radiation damage near grain boundaries via interstitial emission, Science 327 (2010) 1631.
[19] M. Panizo-Laiz, P. Díaz-Rodríguez, A. Rivera, G. Valles, I. Martín-Bragado, J.M. Perlado, F. Munnik, R. González-Arraba, Experimental and computational studies of the influence of grain boundaries and temperature on the radiation-induced damage and hydrogen behavior in tungsten, Nucl. Fusion 59 (2019) 086055.
[20] G. Ackland, Controlling radiation damage, Science 327 (2010) 1587.

[21] H. Zhao, X. Zeng, X. Yang, W. Chen, J. Wu, Investigation of the temperature effect on the primary radiation damage near the grain boundary in tungsten using Molecular dynamics simulations, Nucl. Instrum. Methods Phys. Res. B 476 (2020) 32.
[22] I.J. Beyerlein, A. Caro, M.J. Demkowicz, N.A. Mara, A. Misra, B.P. Uberuaga, Radiation damage tolerant nanomaterials, Mater. Today 16 (2013) 443.
[23] O.V. Ogorodnikova, Y. Gasparyan, V. Efimov, Ł. Ciupiński, J. Grzonka, Annealing of radiation-induced damage in tungsten under and after irradiation with 20 MeV self-ions, J. Nucl. Mater. 451 (2014) 379.
[24] E. Markina, M. Mayer, A. Manhard, T. Schwarz-Selinger, Recovery temperatures of defects in tungsten created by self-implantation, J. Nucl. Mater. 463 (2015) 329.
[25] A. Založnik, S. Markelj, T. Schwarz-Selinger, Ł. Ciupiński, J. Grzonka, P. Vavpetič, P. Pelicon, The influence of the annealing temperature on deuterium retention in self-damaged tungsten, Phys. Scr. T167 (2016) 014031.
[26] S. Sakurada, K. Yuyama, Y. Uemura, H. Fujita, C. Hu, T. Toyama, N. Yoshida, T. Hinoki, S. Kondo, M. Shimada, D. Buchenauer, T. Chikada, Y. Oya, Annealing effects on deuterium retention behavior in damaged tungsten, Nucl. Mater. Energy 9 (2016) 141.
[27] M.J. Simmonds, Y.Q. Wang, J.L. Barton, M.J. Baldwin, J.H. Yu, R.P. Doerner, G.R. Tynan, Reduced deuterium retention in simultaneously damaged and annealed tungsten, J. Nucl. Mater. 494 (2017) 67.
[28] M. Pečovnik, S. Markelj, M. Kelemen, T. Schwarz-Selinger, Effect of D on the evolution of radiation damage in W during high temperature annealing, Nucl. Fusion 60 (2020) 106028.
[29] M.J. Simmonds, T. Schwarz-Selinger, M.I. Patino, M.J. Baldwin, R.P. Doerner, G.R. Tynan, Reduced defect recovery in self-ion damaged W due to simultaneous deuterium exposure during annealing, Nucl. Fusion 62 (2022) 036012.
[30] D. Dellasega, G. Merlo, C. Conti, C.E. Bottani, M. Passoni, Nanostructured and amorphous-like tungsten films grown by pulsed laser deposition, J. Appl. Phys. 112 (2012) 084328.
[31] www.srim.org.
[32] M.J. Baldwin, D. Nishijima, M.I. Patino, G. Gunner, T. Lynch, F. Chang, M.J. Simmonds, A. Založnik, S. Moore, B. Schwendeman, R. Ciamacco, R.P. Doerner, G.R. Tynan, Pisces-RF: A helicon-plasma based linear-device for the study of fusion relevant plasma-materials-interactions, Nucl. Mater. Energy 36 (2023) 101477.
[33] D. Nishijima, M. Tokitani, D. Nagata, T. Schwarz-Selinger, A. Založnik, F. Chang, R.P. Doerner, M.I. Patino, M.J. Simmonds, M.J. Baldwin, G.R. Tynan, Deuterium supersaturated surface layer in tungsten: ion energy dependence, Nucl. Fusion 63 (2023) 126003.
[34] S. Nagata, T. Takahiro, S. Horiike, S. Yamaguchi, Retention and release of deuterium implanted in W and Mo, J. Nucl. Mater. 266–269 (1999) 1151.
[35] O.V. Ogorodnikova, J. Roth, M. Mayer, Deuterium retention in tungsten in dependence of the surface conditions, J. Nucl. Mater. 313–316 (2003) 469.
[36] O.V. Ogorodnikova, Fundamental aspects of deuterium retention in tungsten at high flux plasma exposure, J. Appl. Phys. 118 (2015) 074902.
[37] M. Zibrov, S. Ryabtsev, Y. Gasparyan, A. Pisarev, Experimental determination of the deuterium binding energy with vacancies in tungsten, J. Nucl. Mater. 477 (2016) 292.
[38] M. Zibrov, The Influence of Radiation, Mechanical, and Plasma-Induced Damage on Deuterium Retention inTungsten (Ph.D. thesis), Technische Universität München, 2018.
[39] R. González-Arrabal, M. Panizo-Laiz, N. Gordillo, E. Tejado, F. Munnik, A. Rivera, J.M. Perlado, Hydrogen accumulation in nanostructured as compared to the coarse-grained tungsten, J. Nucl. Mater. 453 (2014) 287.
[40] S. Markelj, T. Schwarz-Selinger, M. Kelemen, E. Punzón-Quijorna, J. Zavašnik, A. Šestan, D. Dellasega, G. Alberti, M. Passoni, The effect of nanocrystalline microstructure on deuterium transport in displacement damaged tungsten, Nucl. Mater. Energy 37 (2023) 101509.
[41] M.W. Thompson, The damage and recovery of neutron irradiated tungsten, Phil. Mag. 5 (1960) 278.
[42] V.N. Bykov, G.A. Birzhevoi, M.I. Zakharova, V.A. Solov'ev, Nature and thermal stability of radiation defects in single-crystal tungsten, At. Energ. 33 (1972) 930.
[43] F. Ferroni, X. Yi, K. Arakawa, S.P. Fitzgerald, P.D. Edmondsone, S.G. Roberts, Hight temperature annealing of ion irradiated tungsten, Acta Mater. 90 (2015) 380.
[44] A. Debelle, M.F. Barthe, T. Sauvage, First temperature stage evolution of irradiation-induced defects in tungsten studied by positron annihilation spectroscopy, J. Nucl. Mater. 376 (2008) 216.
[45] J. Heikinheimo, K. Mizohata, J. Räisänen, T. Ahlgren, P. Jalkanen, A. Lahtinen, N. Catarino, E. Alves, F. Tuomisto, Direct observation of mono-vacancy and self-interstitial recovery in tungsten, APL Mater. 7 (2019) 021103.
[46] K. Schmid, V. Rieger, A. Manhard, Comparison of hydrogen retention in W and W/Ta alloys, J. Nucl. Mater. 426 (2012) 247.
[47] M. Zibrov, W. Egger, J. Heikinheimo, M. Mayer, F. Tuomisto, Vacancy cluster growth and thermal recovery in hydrogen-irradiated tungsten, J. Nucl. Mater. 531 (2020) 152017.